Electrocatalysis

How to cite: *Angew. Chem. Int. Ed.* **2022,** *61,* e202211543
International Edition: doi.org/10.1002/anie.202211543
German Edition: doi.org/10.1002/ange.202211543

Surface Boron Modulation on Cobalt Oxide Nanocrystals for Electrochemical Oxygen Evolution Reaction

*Mingquan Yu, Claudia Weidenthaler, Yue Wang, Eko Budiyanto, Ezgi Onur Sahin, Minmin Chen, Serena DeBeer, Olaf Rüdiger, and Harun Tüysüz**

Abstract: Herein, we show that coupling boron with cobalt oxide tunes its structure and significantly boost its electrocatalytic performance for the oxygen evolution reaction (OER). Through a simple precipitation and thermal treatment process, a series of Co–B oxides with tunable morphologies and textural parameters were prepared. Detailed structural analysis supported first the formation of an disordered and partially amorphous material with nanosized Co_3BO_5 and/or $Co_2B_2O_6$ being present on the local atomic scale. The boron modulation resulted in a superior OER reactivity by delivering a large current and an overpotential of 338 mV to reach a current density of 10 mA cm^{-2} in 1 M KOH electrolyte. Identical location transmission electron microscopy and in situ electrochemical Raman spectroscopy studies revealed alteration and surface re-construction of materials, and formation of CoO_2 and (oxy)hydroxide intermediate, which were found to be highly dependent on crystallinity of the samples.

Introduction

Electrochemical water splitting offers a means to store intermediate electricity from renewable energy sources like solar, wind, and hydropower.[1] It is an efficient and sustainable technology with the capacity to store enormous amount of energy in chemical bonds, as a clean alternative to fossil fuels.[2] In a water electrolyzer, hydrogen is generated at the cathode, accompanied with the formation of oxygen as the only by-product at the anode, namely the oxygen evolution reaction (OER). OER is kinetically sluggish, as it involves four electron transfer steps and oxygen-oxygen bond formation, regarded as the bottleneck of water electrolysis systems.[3] Design of OER electrocatalysts with high efficiency is thus an imperative mission to both fundamental research and industrial applications under the framework of a hydrogen economy.[4]

Iridium and ruthenium oxides are generally considered as benchmark OER catalysts, but the scarcity and high cost of noble metals impede their practical applications, especially in large-scale water electrolyzers.[3] Decades of research efforts have explored a wide range of promising alternatives based on earth-abundant transition metals (TM, e.g., Fe, Co, Ni, Mn),[3,5] mostly in the form of TM oxides,[6] TM (oxy)hydroxides,[7] and perovskites.[8] As a new category of OER catalysts, TM-based compounds containing some nonmetals (like N, P and S) and metalloids (like B and As) have recently attracted special interest.[9] It has been widely reported that introducing such guest elements accelerates charge transfer rates between different elements. In addition, it modifies the electronic structure of active TM centers, which effectively lowers the kinetic energy barrier of the electrochemical process.[10] Therefore, the combination of TM with some other elements could lead to an exceptionally good activity towards OER as a result of synergistic effects.

TM based catalysts, containing phosphorous (P) and/or boron (B), have been reported to show remarkable OER activities in neutral and alkaline medias.[10b,11] Since Nocera et al. explored the potential of cobalt phosphate (Co–Pi) as OER catalyst in an artificial water-splitting system,[12] a series of TM–Pi catalysts have been reported with outstanding catalytic performance, such as $Li_{2x}MnP_2O_7$,[13] $Na_2CoP_2O_7$,[14] $Co_3(PO_4)_2$,[15] and $FePO_4$.[16] In addition, various TM–P catalysts in the phase of phosphide, like $(Ni_xFe_{1-x})_2P$,[17] $Co_{0.93}Ni_{0.07}P_3$,[18] and $Ni_2P(O)/Fe_2P(O)$,[19] have been discovered as pre-catalysts for OER with metallic bulk and reactive oxy/hydroxide surfaces. On the other hand, TM–B compounds, as the analog of TM–P catalysts, are expected to possess similar OER activity.[20] It has been shown that incorporation of more electronegative boron into nickel and cobalt oxides reduces the oxidation reaction energy barrier under an applied bias and facilities the charge transfer.[20a,21] However, design of TM–B catalysts with high surface area and electrocatalytic activity has been challenging due to their easy aggregation during the synthesis, low stability at high pH regime, and humble understanding of their catalytic functionalities.[9a,10b]

[*] Dr. M. Yu, Priv.-Doz. Dr. C. Weidenthaler, Y. Wang, E. Budiyanto, Dr. E. Onur Sahin, Priv.-Doz. Dr. H. Tüysüz
Max-Planck-Institut für Kohlenforschung
Kaiser-Wilhelm-Platz 1, D-45470 Mülheim an der Ruhr (Germany)
E-mail: tueysuez@kofo.mpg.de

M. Chen, Prof. Dr. S. DeBeer, Dr. O. Rüdiger
Max Planck Institute for Chemical Energy Conversion
Stiftstrasse 34–36, D-45470 Mülheim an der Ruhr (Germany)

© 2022 The Authors. Angewandte Chemie International Edition published by Wiley-VCH GmbH. This is an open access article under the terms of the Creative Commons Attribution Non-Commercial License, which permits use, distribution and reproduction in any medium, provided the original work is properly cited and is not used for commercial purposes.

 © 2022 The Authors. Angewandte Chemie International Edition published by Wiley-VCH GmbH

Herein, we prepare a series of Co–B oxide nanostructures with high surface areas and tunable morphologies through a simple precipitation method by using $NaBH_4$ simultaneously as a reducing agent and boron precursor. A post thermal treatment causes the segregation of the partly amorphous cobalt borates into amorphous boron oxide and crystalline Co_3O_4. The amorphous boron oxide phase was found to not only assist confinement of cobalt oxide particles, it also affected its crystallization. As a result, a very good OER performance is achieved on Co–B oxides with good stability and durability in high pH alkaline electrolyte. The synergic effect of cobalt and boron resulted in a three-fold enhancement of the OER activity of Co–B oxide electrocatalysts compared to reference ordered mesoporous Co_3O_4 counterpart.

Results and Discussion

Partially amorphous Co–B oxide was prepared by a facile precipitation method using $Co(Ac)_2$ and $NaBH_4$ as cobalt and boron precursors, respectively, see Supporting Information for the experimental details. Inductively coupled plasma optical emission spectroscopy (ICP-OES) analysis revealed a boron/cobalt atomic ratio of 12 % within the synthesized sample. A calcination step was implemented at varying temperatures (from 200 to 550 °C) to crystallize the oxides. The prepared samples are labeled as "Co–B oxide (X)-Y" where X and Y indicate the cobalt precursor and the calcination temperature, respectively. High-resolution transmission electron microscopy (HR-TEM) was used to image the morphology of the as-prepared Co–B oxides. As shown in Figure 1a, as-made sample (Co–B oxide-RT) consists of interconnected nanoparticles, no clear lattice fringes can be observed on the aggregated particles, suggesting the highly distorted, almost amorphous nature of the precipitates at room temperature. Applying heat treatment induced crystallization and dehydration processes on the partially amorphous Co–B oxide, leading to the formation of crystallites, as well as grain boundaries in between individual particles (Figure 1b, c and Figure S1). Partially crystalline particles were observed on the oxide calcined at intermediate temperatures like 300 °C and 400 °C. Increasing the calcination temperature accelerated the growth of crystallites, with clear lattice fringes exhibited on all particles that were calcined at 550 °C as seen in Figure 1c. A closer examination at higher magnification further allows the interplanar spacing to be measured at 0.28 nm, corresponding to the (220) lattice fringes of Co_3O_4 spinel, respectively. The crystalline particles did not sinter significantly into very large bulk particles even after 4 hours of thermal treatment at 550 °C. Despite some aggregation upon the thermal treatment, the crystallite sizes of the composite material were mainly below 10 nm with irregular shapes (Figure S2). Such high temperature normally produces large particles when the particles are not confined within rigid solid materials.[22] Introducing B appears to play an important role in suppressing rapid growth of crystalline Co_3O_4 particles into bulk material.

The textural parameters of these particulate Co–B oxides were determined by nitrogen physisorption measure-

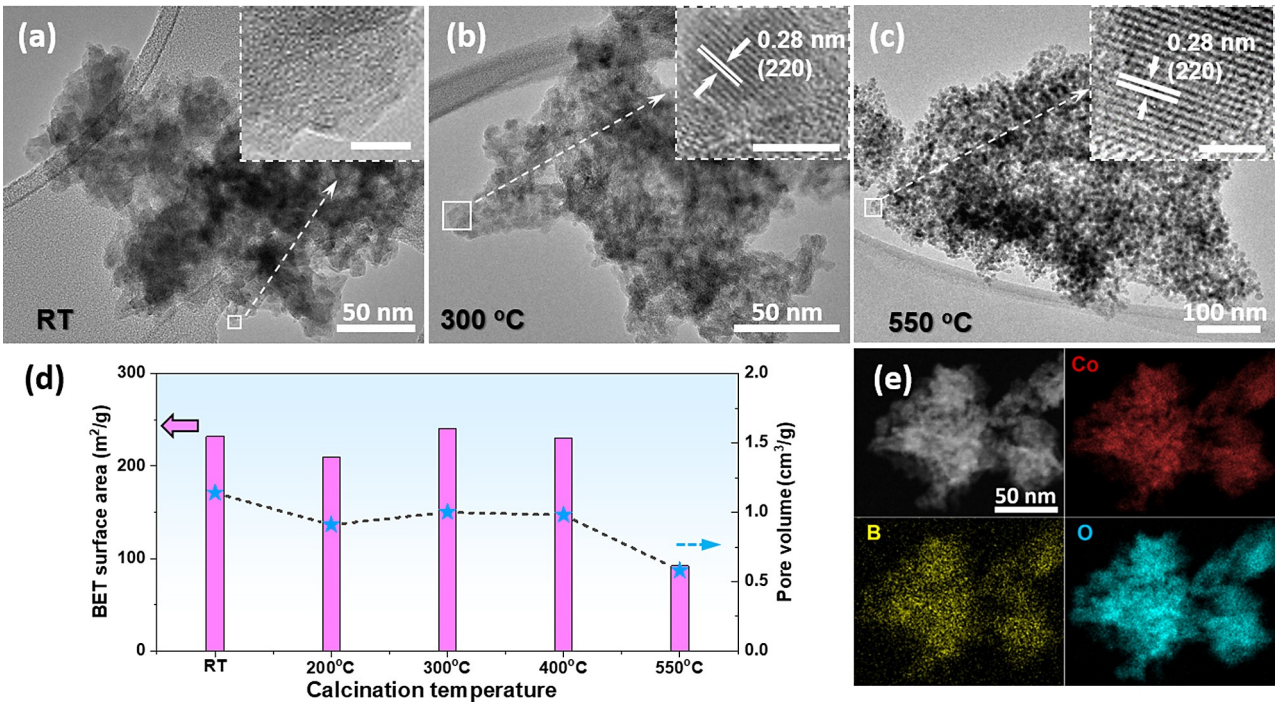

Figure 1. a–c) High-resolution TEM images of Co–B oxides prepared at different temperatures (RT, 300 and 550 °C, respectively). Insets are the corresponding close-up of the marked rectangles, scale bars in insets are 2 nm. d) Summarized values of the BET surface area of (left axis) and pore volume (right axis) of Co–B oxides. e) HR-SEM image and corresponding elemental mapping of Co, B and O of Co–B oxide-300

© 2022 The Authors. Angewandte Chemie International Edition published by Wiley-VCH GmbH

ments. In Figure S3, the isotherms show the porous structures of Co–B oxides with and without heat treatment. As summarized in Figure 1d and Table S1, these oxides possess large BET surface areas and high pore volumes. The porous structure remained on Co–B oxides after calcination at up to 400 °C by maintaining a BET surface area larger than 200 $m^2 g^{-1}$ and a pore volume of around 1 $cm^3 g^{-1}$. This clearly outperforms the values obtained for ordered mesoporous Co_3O_4 prepared by an energy and time-intensive nanocasting process.[22a] Further increase of the temperature to 550 °C causes partly shrinkage of the structure and a decrease in the surface area and pore volume (Figure 1d). As seen in Figure 1e, the high-resolution scanning electron microscopy (HR-SEM) and corresponding elemental mapping images show a uniform distribution of O, Co, and B over the Co–Bo oxide-300 sample.

In order to investigate the crystal structure and arrangements of boron, as well as its potential protective effect on the cobalt oxide, a detailed structural characterization was performed on the as-made sample (Co–B oxide-RT) and after its calcination at 300 °C (Co–B oxide-300) and 550 °C (Co–B oxide-550). and ordered mesoporous Co_3O_4 spinel that was replicated from KIT-6 silica (further denoted as KIT-6_Co_3O_4) as the reference material. As seen in Figure 2a, the X-ray diffraction (XRD) patterns indicate the partially amorphous nature of the Co–B oxide-RT sample. Two broad and asymmetric reflections are characteristic for stacking faults and point to a highly distorted structure of the starting material. The XRD pattern collected after calcination at 300 °C shows that the sample has started to change and Co_3O_4 has crystallized. The reflections become sharper when the temperature is increased to 550 °C indicating crystal growth. No additional phases associated with any crystalline boron species could be identified during the calcination process. In fact, the diffractogram of the sample calcined at 550 °C fits well to the reference KIT-6_Co_3O_4 structure that has been calcined at a similar temperature.

X-ray photoelectron spectroscopy (XPS) was further carried out to check the surface composition and electronic structure of KIT-6_Co_3O_4 and Co–B oxide samples. The survey XPS spectrum in Figure S4 exhibits a clean surface that is composed of Co, B, and O, which is also supported by bulk energy-dispersive X-ray (EDX) analysis (Figure S5). The analysis of the Co 2p core level XPS spectrum is very complex. In addition to the spin-orbit couple $2p_{3/2}$ and $2p_{1/2}$, a strong background signal, the overlap with Auger peaks (A1), and the appearance of satellite peaks from multi-electron excitation (shake-up peaks, S1 and S2), and multiplet splitting contribute to the measured spectrum.[23] Changes of the stoichiometry and therewith the oxidation state reflecting changes from the rock-salt CoO to the spinel Co_3O_4 are accompanied by changes of the intensity ratios of

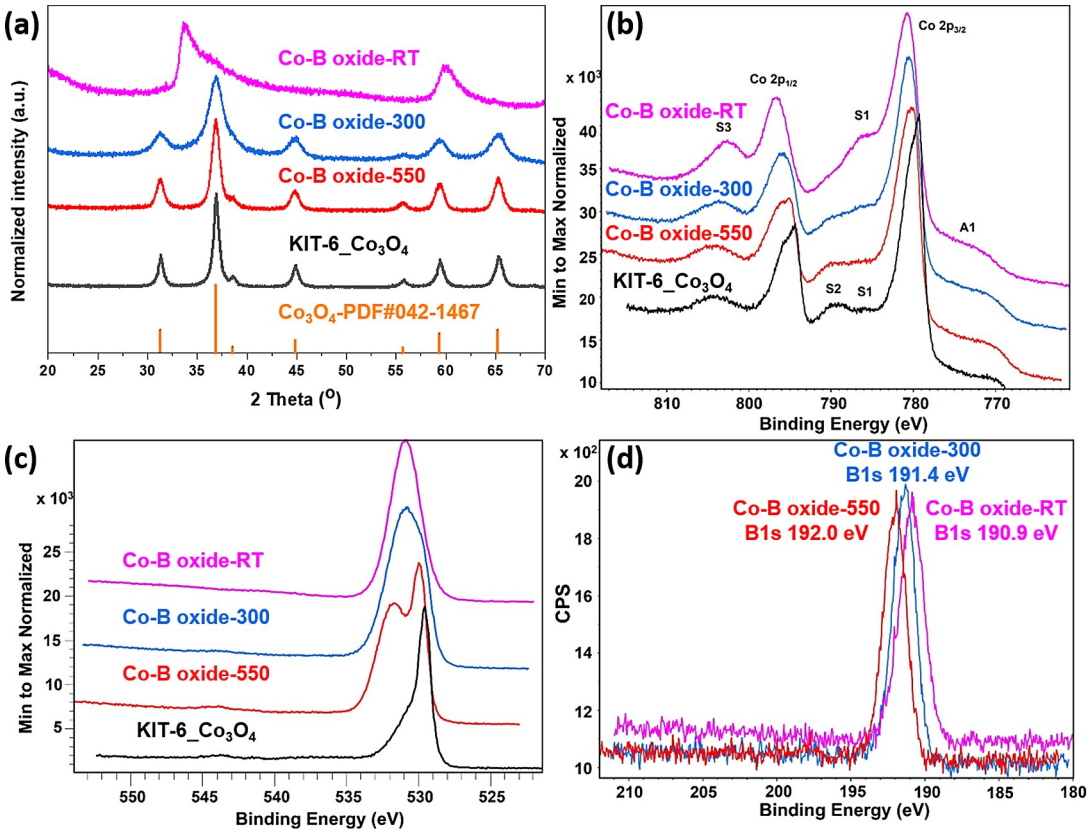

Figure 2. a) XRD patterns, b) XPS spectra of Co 2p and c) O 1s core emission spectra of KIT-6_Co_3O_4 reference, Co–B oxide-RT, Co–B oxide-300 and Co–B oxide-550 samples. d) XPS spectra of B 1s region of Co–B oxide-RT, Co–B oxide-300, Co–B oxide-550 samples.

© 2022 The Authors. Angewandte Chemie International Edition published by Wiley-VCH GmbH

the O 1s/Co 2p photoemissions, as well as of the oxygen and Co Auger lines.[24]

As seen in Figure 2b, the binding energies of the Co 2p peaks are clearly different among the Co–B oxide samples and KIT-6_Co_3O_4 counterpart, suggesting a different Co^{2+} and Co^{3+} content on their surface. The Co2p core-level spectrum of KIT-6_Co_3O_4 reference sample contains the photoemissions of both Co^{3+} and Co^{2+}. The $Co2p_{3/2}$ peak belonging to Co^{3+} appears at 779.4 eV while $Co2p_{3/2}$ indicating Co^{2+} has the maximum at 780.7 eV. The shake-up peak S1 at ≈785 eV is characteristic for Co^{2+} while S2 at ≈789 eV is assigned to Co^{3+}. For boron-free KIT-6_Co_3O_4, the spectrum shows clearly that the intensity of the S2 peak is higher than that of the S1 peaks, which would be expected for the electronic structure of the spinel. The broad features at the lower binding energy side labelled with A1 represents the Co Auger peaks, which are not further resolved.

For the as-made sample of Co–B oxide-RT, the intense S1 satellite indicates Co^{2+} as the dominant oxidation state (Figure 2b). For Co–B oxide-300, the intensity of the S1 peak is still high, which indicates that the amount of Co^{2+} on the surface is dominating. The Co–B oxide-550 displays a XPS spectrum comparable to boron-free KIT-6_Co_3O_4, supporting the similarity of the surface structures for both samples. However, even if the Co 2p core level spectrum of Co–B oxide-550 (Figure 2b) looks analogous to that of KIT-6_Co_3O_4, fitting the spectra reveals some intensity differences of the S1 and S2 satellite peaks (Figure S6). The S1 shake-up peak for Co–B oxide-550 is higher indicating the presence of more Co^{2+} on the surface than expected for Co_3O_4. Overall, the XPS analysis revealed that the sample surface after synthesis is mainly composed of Co^{2+}, while the amount of Co^{2+} is decreased upon the thermal treatment. The fitted spectra of the Co $2p_{3/2}$ branch show differences between the ratios of the S1 and S2 satellite peaks. The intensity of the S2 satellite increases with higher calcination temperatures due to the oxidation of Co^{2+} to Co^{3+} (Figure S6). Nevertheless, even after calcination at 550 °C, there is still surplus amount of Co^{2+} on the surface when compared to KIT-6 Co_3O_4. This indicates that the presence boron species does not only influence confinement and sintering of cobalt oxide particles, it also affects crystallization and surface structure of the cobalt oxide.

The O 1s spectrum of the reference KIT-6_Co_3O_4 is assigned to the contributions of four different oxygen species with S0 at 529.6 eV as main lattice oxygen peak (Figure S7). The other peaks are discussed controversially in literature as non-stoichiometric near surface oxygen, adsorbed hydroxyls, OH^-, or cobalt hydroxides.[23,25] Co–B oxide-RT shows only one broad photopeak at 530.9 eV which cannot be assigned to one of those mentioned species. As will be discussed in the following, the local structure of the partially amorphous sample can be explained by different cobalt boron oxide phases, with structures different to that of Co_3O_4 spinel. Temperature treatment at 300 °C leads to the formation of more defined oxygen species with a new maximum showing up at 529.8 eV. The sample calcined at 550 °C (Co–B oxide-550) has a defined core level peak with a chemical shift of 529.9 eV corresponding to the O 1s core level peak as observed for the reference KIT-6_Co_3O_4 sample. The O 1s signals at higher binding energies gain a lot of intensity and the components at 531.2 and 532.2 eV become more significant as seen in Figure 2c. The peak at 532.2 eV could be assigned to B_2O_3,[26] which verifies presence of also boron oxide alongside cobalt oxide. Figure 2d illustrates the B 1s photo peaks of all three boron containing samples. The peak position shifts systematically from 190.9 eV for Co–B oxide-RT to 192.0 eV for Co–B oxide-550 with the higher binding energy being characteristic for B_2O_3.[27] This temperature-dependent shift is a clear indication for the structural rearrangement during the calcination, which will be discussed in more detail below.

As discussed above, the as-made Co–B oxide-RT is partially amorphous (verified by TEM and XRD analyses). For this reason, alternative tools are required to enable the analysis on the local atomic scale and by which also the temperature-dependent crystallization can be monitored. Total scattering experiments are suitable for the analysis of local structures not only of the short-range but also intermediate- and long-ranges.[28] The crystallization of Co–B oxide-RT sample was further studied by in situ temperature-dependent total scattering experiments and subsequent pair distribution function (PDF) analysis (Figure 3). The first comparison of the measured PDF data of Co–B oxide-RT reveals that the data do not fit to Co_3O_4 or B_2O_3 structures (Figure S8). The comparison with simulated PDFs of CoO, CoO(OH) and $Co(OH)_2$ indicates matches of some of the measured atom pairs with the simulations (Figure S8). However, a refinement based on pure Co-oxides or hydroxides failed. Next, simulations and subsequent refinements of the PDF data with different Co–B-oxide structures were performed, whereby a good match with the structure data of Co_3BO_5 was identified (Figure S9a). The refinement gets better if a second Co–B-oxide, $Co_3B_2O_6$, is included (Figure S9b). A further combination with $Co(OH)_2$ leads to only a slight improvement when three structures are considered for refinement (Figure S9c–d). After calcination at 550°C in air, a clear alteration of the structure was observed as shown by the fitting of in situ PDF data in Figure S10. A good refinement was obtained with only cobalt oxide phases (i.e. Co_3O_4 and CoO), indicating the decomposition of Co–B oxide into cobalt oxide and boron oxide (low scattering contract and therefore almost invisible) as a result of the high temperature treatment.

The alteration of the main atom-pair correlation observed for the experimental PDF obtained at room temperature is caused by the Co–O distances in the CoO_6-octahedra at ≈2.1 Å (labelled as B in Figure 3), followed by the Co–Co correlations between neighboring, edge-sharing octahedra at about 3.1 Å (D) as shown in Figure 3. Since most of the octahedra in this structure share edges, the Co–Co correlation from corner-sharing octahedra at ≈3.5 Å is low in intensity. The broad atom correlation with a maximum at ≈1.4 Å is related to B–O distanced within the planar BO_3 groups (A). The pair correlation at ≈2.4 Å can be associated either to Co–B in Co_3BO_5 or O–O distances between neighbored octahedra. The crystal structure of

 © 2022 The Authors. Angewandte Chemie International Edition published by Wiley-VCH GmbH

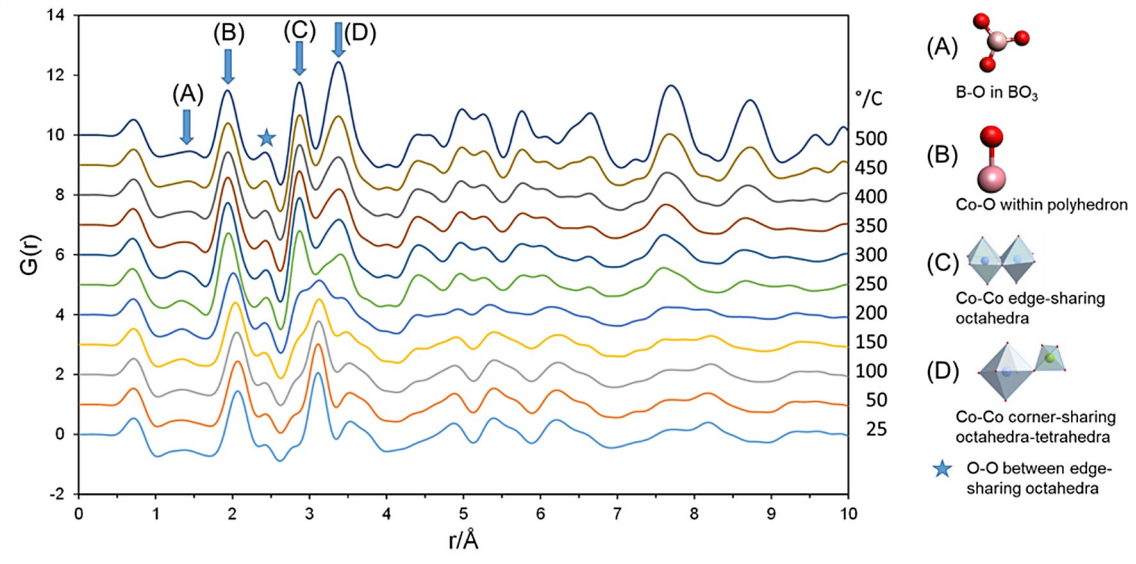

Figure 3. The temperature-dependent in situ PDF data obtained for Co–B oxide-RT plotted in the range between RT and 500 °C.

Co_3BO_5 contains Co in 2+ and 3+ oxidation states and both cations are located in octahedral coordination. Boron is in the usual planar, threefold coordination. The structure of $Co_3B_2O_6$ contains only Co^{2+} cations in octahedral coordination and B in the threefold planar coordination as illustrated in Figure S11. The growth and crystallization process were further monitored using in situ PDF analysis in the temperature range between RT and 500 °C. Initially, the as-prepared precipitant consisted of mainly cobalt boron oxides with crystallite sizes below 1 nm. Therefore, no defined reflections can be observed in the conventional diffraction patterns. No noteworthy differences in the experimental PDFs are observed up to 150 °C. At 150 °C, significant changes start to appear in the short-range order between 2.5 and 4 Å.

These changes can be attributed to the rearrangement of the octahedra, the formation of tetrahedra and an increasing number of corner- instead of edge-sharing polyhedra. Upon further heating, more defined PDF peaks appear and increasing the heating temperature above 250 °C causes splitting of the peak at 3.2 Å into two peaks. These can be assigned to Co–Co atom-pairs between edge-sharing octahedra (C) and corner-sharing octahedra and tetrahedra (D), which gives hint for the formation of the Co_3O_4 structure. The B–O bond (A, in Figure 3) belongs to the planar coordinated BO_3 group in the cobalt boron oxide structures. The transformation of Co_3BO_5 and/or $Co_3B_2O_6$ into Co_3O_4 takes place at temperatures above 150 °C. The structure of the boron-containing phase is not easy to assign because both boron and oxygen are weak scatterers. Only the pair correlation with a maximum between 1.4–1.5 Å can be related to B–O in planar BO_3 groups. Since the threefold coordination of boron by oxygen is maintained in structures such as B_2O_3, no significant change is observed in the B–O bond length over the measured temperature range. A direct comparison of the experimental PDF data obtained at RT and 500 °C shows significant changes (Figure 3). The first main atom-pair correlation has shifted from 2.1 to 1.9 Å, which corresponds to Co–O distances within the CoO_4 tetrahedron in the Co_3O_4 spinel structure. The structures analyzed at room temperature do not contain significant amounts of Co–O tetrahedra and the tetrahedra only form during thermal treatment. The second maximum has shifted from 3.1 to 2.9 Å which corresponds to Co–Co distances of edge-sharing octahedra. The distance at 3.4 Å is related to Co_{tet}–Co_{oct}. This further confirmed major structural rearrangement upon the thermal treatment.

The structure of Co sites in the bulk was further investigated with a combination of X-ray absorption (XAS) and emission (XES) spectroscopies. The Co L-edge XAS is sensitive to the oxidation and spin state of the sample, as well as the geometry. The L_3 edges (Figure 4a) show a clear decrease in the low energy side of the peak as the calcination temperature is increased, indicating a higher average oxidation state. The shape of the Co–B oxide-RT is consistent with a Co^{2+} in a O_h coordination, while the KIT-6_Co_3O_4 spinel is consistent with the expected Co^{3+}/Co^{2+} mixture.[29] The spectra of the 300 °C and 550 °C calcined samples can be easily deconvoluted as a combination of the pristine Co_3O_4 and the starting as-made material (Figure S12). The Co–B oxide-300 sample can be deconvoluted to a mixture of 60 % pristine Co_3O_4 and 40 % starting material, while the conversion value for the Co–B oxide-550 was increased to 80 % at the calcination temperature of 550 °C. This is consistent with the findings from the XPS analysis whereby high stoichiometric amount of Co^{+2} species was detected on the surface of Co–B oxide-550 in comparison with the KIT-6_Co_3O_4 spinel sample.

The Co K-edges (Figure 4b) parallel the trends observed at the Co L-edge, with the Co–B oxide-RT sample appearing most reduced (based on the rising edge position) followed by the Co–B oxide-300 and Co–B oxide-550

 © 2022 The Authors. Angewandte Chemie International Edition published by Wiley-VCH GmbH

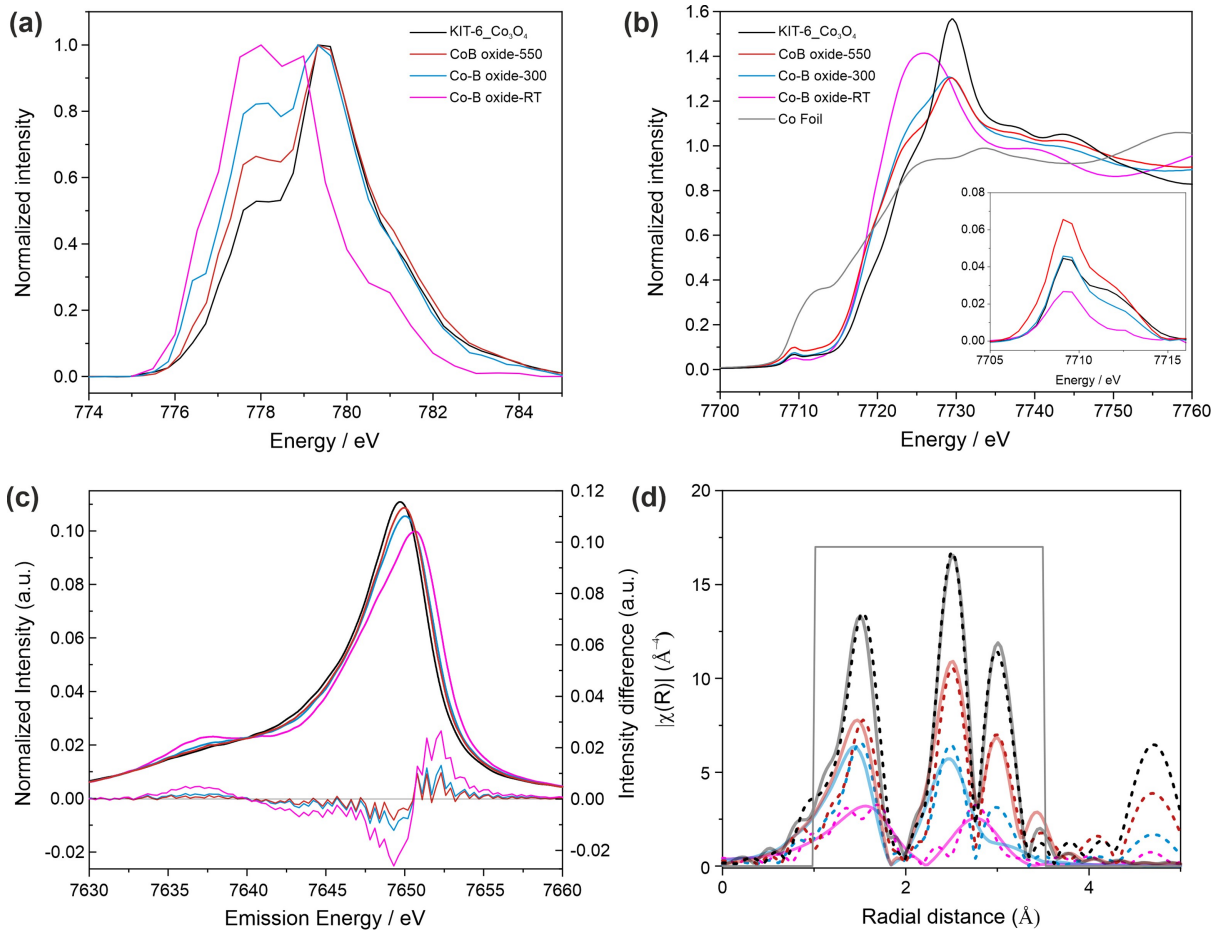

Figure 4. Co L-edge (a), K-edge (b) XAS and Kβ XES (c) spectra of Co–B oxide-RT, Co–B oxide-300 and Co–B oxide-550 and KIT-6_Co_3O_4. The inset in panel (b) shows the baseline corrected pre-edge region in detail including Co foil as reference. The subtracted spectra XES (Co–B oxide minus pristine Co_3O_4) is shown at the bottom of the spectra to highlight the differences. d) Real part of the Fourier transformed Co K-edge EXAFS spectra of Co–B oxides (experimental data as dotted trace and fitting as solid trace) at RT, calcined at 300 and 550 °C and KIT-6_Co_3O_4.

samples. The KIT-6_Co_3O_4 reference sample appears to highest energy, indicating it contains the largest fraction of oxidized cobalt (Figure 4b) as also verified by XPS study. The Kβ XES corresponding to 3p→1s emission, reflects the electronic configuration of the 3d orbitals due to the strong 3p–3d exchange coupling, which results in a splitting of the Kβ line into the Kβ' and $K\beta_{1,3}$ lines.[30] A larger splitting between these two lines reflects a higher spin of the emitting ion.[31] Consistent with a Co^{2+} high-spin (HS) in O_h geometry ($S=3/2$), the as-made Co–B oxide-RT sample has the most intense Kβ', while the samples that are calcined at 300 and 550 °C possess increased amount of high spin compared to the KIT-6_Co_3O_4. The latter has a spectrum dominated by the Co^{3+} low-spin (LS, $S=0$), as we showed in a previous work.[32] The spectra of the Co–B oxide-300 and Co–B oxide-550 oxides can also be reproduced by combining the RT and the KIT-6_Co_3O_4 spectra with the same ratio as used for the L-edges (Figure S12). The extended X-ray absorption fine structure (EXAFS) region of the XAS can be used to obtain additional structural information about the coordination of the absorbing ion. The R-space spectra shown in Figure 4d shows how the three characteristic intense features of the Co_3O_4 loose intensity for the Co–B oxide-300 and Co–B oxide-550 samples. The spectrum of the KIT-6_Co_3O_4 reference sample can be fitted with a simple four path model based on the spinel structure, but the fitting parameters degrade dramatically for the Co–B oxide-300.

The decrease in intensity and the increase in the Debye–Waller factors (Table S2) for the spinel fittings indicate an increase in the disorder for the boron-containing samples. This increase in the disorder can help to understand the observed differences in the pre-edge region showed in the inset of the Figure 4b. These quadrupole-allowed but dipole-forbidden 1s→3d transitions gain intensity as the absorbing center deviates from a centrosymmetric geometry (e.g. O_h). While the Co–B oxide-RT sample has a very weak pre-edge signal, the Co–B oxide-300 has almost the same intensity as the KIT-6_Co_3O_4 spinel. This seems contradictory to the L-edge and Kβ spectra deconvolutions, which indicated a 40 % of sample as starting material, and therefore should have a weaker pre-edge. To a lesser extent, the same should apply to the Co–B oxide-550, but for that sample, the pre-edge has even more intensity than the KIT-6_Co_3O_4. This would be

© 2022 The Authors. Angewandte Chemie International Edition published by Wiley-VCH GmbH

consistent with the presence of oxygen deficient Co centers that would break the O_h geometry and therefore increase the intensity of the pre-edge. This might be related to the presence of boron species and their interactions with cobalt oxide, which might play an essential role on the electrocatalytic performance of the material.

After a detailed structural analysis, the electrocatalytic performances of Co–B oxides were investigated for alkaline water electrolysis in 1 M KOH electrolyte by using a glassy carbon as working electrode. Stabilized linear sweep voltammetry (LSV) curves were collected after 50 cycle voltammetry (CV) scans (0.6–1.6 V_{RHE}), these LSV curves are shown in Figure S13a. Two key catalytic parameters, namely, current density at 1.7 V_{RHE} ($j_{@1.7V}$) and required overpotential to reach 10 mA cm^{-2} (η_{10}), are summarized in Figure 5a to evaluate the activity of Co–B oxide catalysts. The OER activity shows an obvious dependence on the calcination temperatures. Partially crystalline oxides calcined at 300 °C and 400 °C show enhanced catalytic performance over amorphous oxides, whereas a higher calcination temperature of 550 °C results in a lower OER activity. The activity enhancement could be attributed to more efficient electron transfer ability of crystalline samples over amorphous counterparts.[20a] On the other hand, the lowest activity on the oxide calcined at 550 °C (Co–B oxide-550) can be ascribed to more than 50 % loss of exposed surface area, although a better conductivity is expected. Among these oxides, Co–B oxide-300 shows the highest OER activity with a high $j_{@1.7V}$ (235 mA cm^{-2}) and low η_{10} (338 mV), which clearly outperform KIT-6_Co_3O_4 (99 mA cm^{-2} and 398 mV) that was replicated by using mesoporous silica as a hard template.[22a,33]

To compare the intrinsic activity of the catalysts, the measured current needs to be normalized to the electrochemical surface area (ECSA) by measuring double layer capacitance (C_{dl}). However, measuring double layer capacitance at non-Faradaic region leads to a high inaccuracy due to the evolution of first anodic peak close to the open circuit

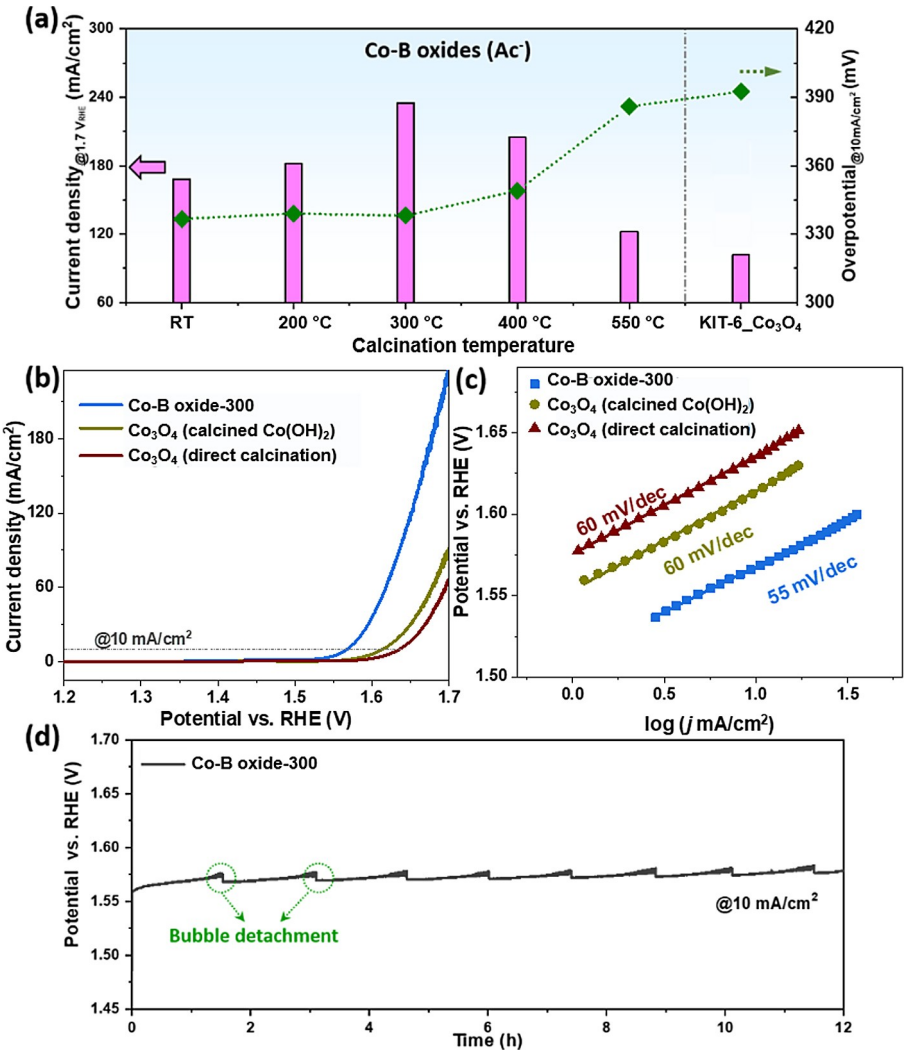

Figure 5. a) Current density at 1.7 V vs. RHE (columns, left axis) and necessary overpotential to reach 10 mA cm^{-2} (lines, right axis) for Co–B oxides prepared at different temperatures, as well as KIT-6_Co_3O_4 for comparison. b) LSV curves and c) corresponding Tafel slopes of three oxide samples prepared at 300 °C d) Chronopotentiometry measurement with fixing current density at 10 mA cm^{-2} for Co–B oxide-300.

© 2022 The Authors. Angewandte Chemie International Edition published by Wiley-VCH GmbH

potential (Figure S13b). Therefore, activity normalized to the corresponding BET surface areas might be a better descriptor for intrinsic activity comparison as suggested by Jaramillo et al.[34] As shown by Figure S13c, all boron-containing samples and reference Co_3O_4 reveal similar current densities at 1.7 V_{RHE} indicating that all samples have a comparable intrinsic activity governed by the cobalt species. On the other hand, boron species provide a protective role that slows down particle aggregation in the boron-contained cobalt phase and enhance the BET surface area as well as providing more exposed cobalt species as active sites.[35] Nevertheless, a clear difference could be observed close to the "visible" onset potential region where samples with higher calcination temperature leads to a slightly lower intrinsic activity. This hints that formation of OER active sites is slower in catalysts with higher degree of crystallinity, which is further supported by the following in situ electrochemical Raman spectroscopy study.

The in situ electrochemical Raman spectroscopy study was further conducted to provide insight into alteration of the electrocatalysts during applied potential bias on selected samples (Co–B oxide-RT, Co–B oxide-300 and Co–B oxide-550). As seen in Figure S14a, Co–B oxide-RT sample has A_{1g} band with broadened and asymmetric peak profile, indicating the distortion on the Co–O bond in the CoO_6-octahedra corresponding to the short-range order properties of this partially crystalline phase.[36] Additionally, a peak at 485 cm^{-1} could be attributed to the E_g band from Co–O–Co vibration on the octahedral sites.[37] A clear peak at 526 cm^{-1} and hump at around 614 cm^{-1} support the presence of a $Co(OH)_2$ phase within the sample.[38] When the sample is immersed in 0.1 M KOH electrolyte solution, an attenuation could be observed for the peak at 526 cm^{-1} due to the dissolution of $Co(OH)_2$ in the alkaline solution.[39] By applying potential bias, new peaks start to evolve from 1.4 V_{RHE} at 467 and 574 cm^{-1} that can be attributed to the E_g and A_{1g} vibrational modes of a disordered CoO_2, respectively (Figure S14b).[37,40] The band corresponding to (oxy)hydroxide intermediate phase that typically shows a broad band at 520–620 cm^{-1} might also overlap with the A_{1g} band from CoO_2.[37,41] The observation of the bands corresponding to CoO_2 with Co^{4+} prior to the "visible" onset potential region of OER supports that the cobalt species at a high oxidation state is the intermediate active phase responsible for OER. The alteration on the Co–O bond in the CoO_6-octahedra could be observed by magnifying the A_{1g} band at around 680–700 cm^{-1} (Figure S14c). A blue-shift to higher wavenumbers could be observed by gradual increase of the applied potential bias. Taking into account the smaller ionic radius of six coordinated Co^{4+} (0.53 Å) compared to Co^{3+}(0.55 Å), the observed trend of the A_{1g} band shift to a higher wavenumber indicates the distortion at the octahedral sites due to the bond compression and charge redistribution due to the oxidation of cobalt species to a higher oxidation state.[36a,37,42]

In situ Raman spectra of Co–B oxide-300 reveals differences at the initial state compared to the aforementioned Co–B oxide-RT (Figure S14d–f). The A_{1g} band of the sample after calcination at 300 °C has lower broadening due to the high degree of long-range order and crystallinity. Upon applied potential bias, the similar surface alteration and blue-shift on A_{1g} band could be observed by the emergence of peaks at 467 and 574 cm^{-1} starting from 1.4 V_{RHE}. However, the intensities of these two peaks are less pronounced compared to the same peaks observed for the Co–B oxide-RT counterpart. The trend of the less intermediate active phase formation is even more pronounced for the Co–B oxide-550 where the band at 520–620 cm^{-1} corresponding to (oxy)hydroxide is barely indistinguishable from the background noise (Figure S14g–i). A similar observation was also observed by Liu et al. where it was found that amorphous or partially amorphous phases can easily form intermediate active sites compared to crystalline counterpart due to the short-range order of the amorphous or partly crystalline structure.[43]

All in all, the in situ electrochemical Raman spectroscopy study indicates that alteration and surface re-construction of materials highly depend on thermal treatment of the as-prepared sample. Lower amount of CoO_2 and (oxy)hydroxide intermediates were formed when the degree of crystallinity of the materials was increased. The results obtained from in situ Raman study go in line with the hypothesis that the formation of OER active site is slower in catalyst with a higher degree of crystallinity, as shown by the measured intrinsic activity normalized by BET surface area.

Identical location TEM study was further carried out to observe the morphology change and surface alteration after OER on the Co–B oxide-300 sample. As shown in Figure S15a–b, the nanoparticulate morphology is mainly retained after OER reaction despite a minor particle collapsed as marked with the white box in the micrograph. Nevertheless, no noticeable bulk particle generation was observed. This points out the protective role of boron to maintain the nanoparticulate size and avoid particle aggregation or Oswald ripening during OER. In addition, the amorphization could be observed on the particle edges (Figure S15c–d) that is originated from the artefact of amorphous CoO_2 or (oxy)hydroxide active sites formation upon applied external potential bias.

The Faradaic efficiency (FE) was further determined for the most active sample Co–B oxide-300 and KIT-6 templated Co_3O_4 reference sample by using a rotating ring-disc electrode (RRDE) method.[44] Both of samples show a FE around 95 % (Figure S16), which indicates that most of the charge was utilized for the oxygen evolution reaction. A slight deviation from 100 % charge utilization might be associated with the alteration of the electrocatalyst and side reactions like carbon oxidation.[45] The Nafion-117 binder used during ink preparation could be responsible as the carbon source.

To study the role of B in more detail, we have further prepared two boron-free Co_3O_4 reference samples that were thermally treated at 300 °C. One sample was synthesized by using NaOH instead of $NaBH_4$, while the other one was obtained via direct calcination of cobalt acetate precursor. As expected, calcination at 300 °C resulted in the formation of highly crystalline Co_3O_4 with sharper reflections for both samples (Figure S17–S18). Additionally, these samples

 © 2022 The Authors. Angewandte Chemie International Edition published by Wiley-VCH GmbH

showed significantly lower BET surface area (Figure S19), illustrating that introducing boron effectively prevents crystallization of cobalt oxide and growth of Co_3O_4 nanoparticles. Consequently, nanoparticulate Co–B oxide-300 shows clear advantages as OER electrocatalysts over pristine cobalt oxide counterparts, with a three-fold increase of the current density and negative shift of more than 46 mV of the overpotential. Moreover, a lower Tafel slope was obtained with Co–B oxide-300 (55 mV dec^{-1}) compared to that of pristine Co_3O_4 (60 mV dec^{-1}, Figure 5c), suggesting the improved OER kinetics in the presence of boron species. As discussed above boron has impacts on the crystal and electronic structure of cobalt oxide, especially the oxidation state of cobalt widely regarded as key for OER.[20a,46] Higher surface area, as well as more reactive Co sites, contribute to a highly competitive catalytic performance of Co–B oxide among benchmark electrocatalysts, as shown in Table S5. Besides the outstanding OER activity, Co–B oxide is very stable over 12 hours stability test (Figure 5d). The SEM-EDX results and inductively coupled plasma atomic emission spectroscopy (ICP-OES) analysis of electrolyte before and after chronopotentiometry measurement (Figure S20 and Table S3) further indicate that the leaching of catalyst is trivial. Durability test of the Co–B oxide-300 sample at severer conditions, a longer time of 48 h or a fixed higher current density of 50 mA cm^{-2}, further demonstrated very good stability and small leaching of the electrocatalyst (Figure S21 and Table S3).

In order to demonstrate the general applicability of this simplified synthesis method, we prepared three other Co–B oxides by choosing different cobalt precursors. Cobalt nitrate, cobalt sulfate, and cobalt chloride are used in each synthesis, with the obtained materials denoted as Co–B oxide (NO_3^-), Co–B oxide (SO_4^{2-}), and Co–B oxide (Cl^-), respectively. By changing cobalt precursors, the morphology of cobalt-boron oxide could be tuned. As shown in Figure 6a–c, at 300 °C calcined Co–B oxide (NO_3^-) possess thin layers of nanosheets to assemble into an open flower like structure while Co–B oxide (Cl^-) has a structure of aggregated nanoparticles. In the case of Co–B oxide

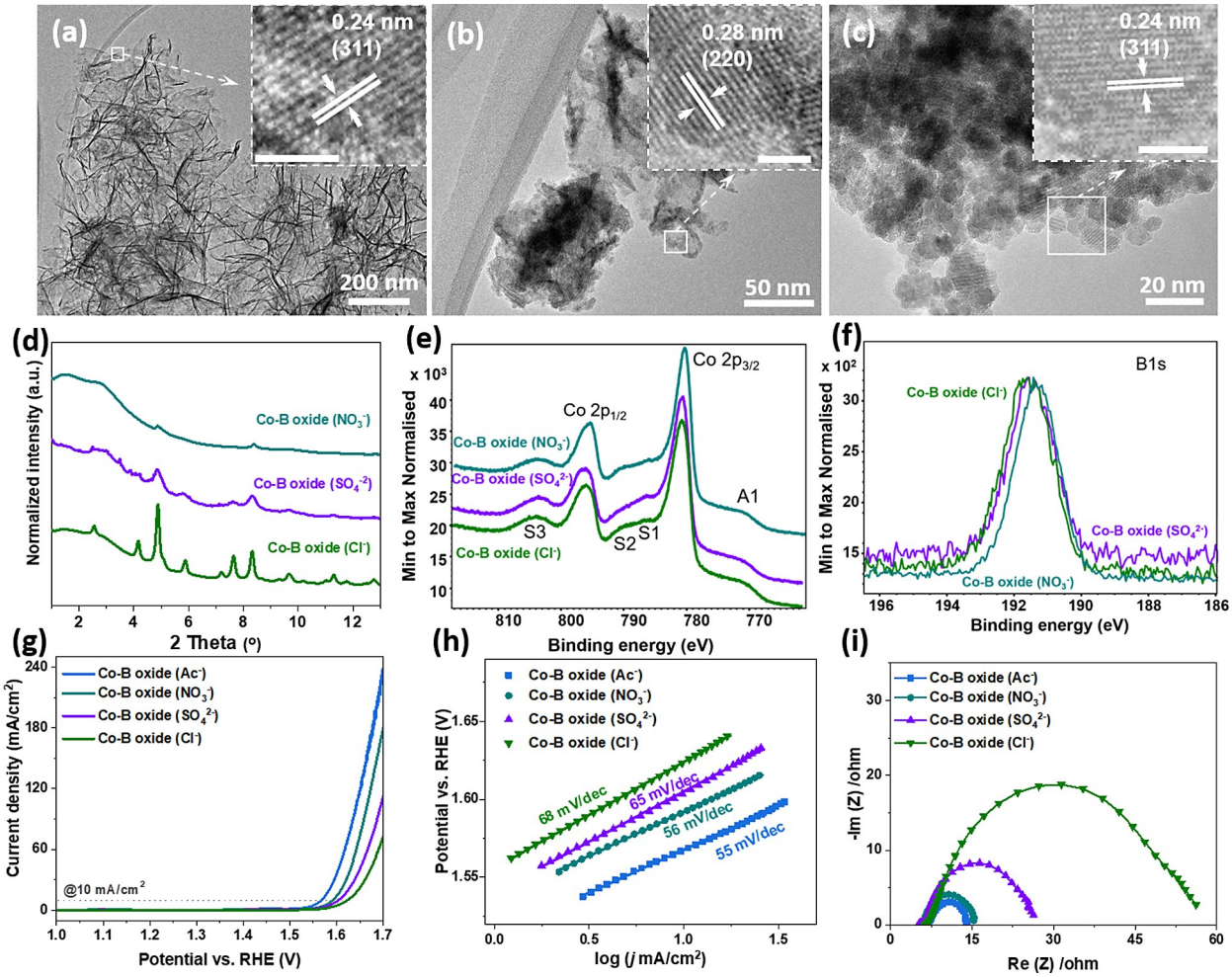

Figure 6. High-resolution TEM images of a) Co–B oxide (NO_3^-), b) Co–B oxide (SO_4^{2-}), and c) Co–B oxide (Cl^-) after calcination at 300 °C. Insets are the corresponding close-up of the marked rectangles, scale bars in insets are 5 nm. d) XRD pattern, e) Co 2p XPS spectra, and f) B 1s XPS spectra of Co–B oxides using different cobalt precursors. g) LSV curves for OER, h) Tafel plots, and i) Nyquist plots of Co–B oxides from different cobalt precursors.

© 2022 The Authors. Angewandte Chemie International Edition published by Wiley-VCH GmbH

(SO_4^{2-}), a hybrid structure that is similar to the transition state between the other two oxides is obtained. These results are consistent with the previous study where sheet-like and particulate structures were prepared by varying precursors under argon atmosphere.[47] Calcination at 300 °C crystallized these oxides to a certain degree. Co–B oxide (NO_3^-) and Co–B oxide (SO_4^{2-}) were partially crystalline whereas large crystals were found for Co–B oxide (Cl^-) sample. This is further supported by synchrotron XRD data by taking into account the reflection intensity and peak broadening of the XRD data (Figure 6d). Due to the difference in morphology, particle size and crystallinity, those obtained oxides showed diverse textural parameters. As shown in Figure S22 and Table S4, the Co–B oxide (NO_3^-) possesses a very large surface area (240 $m^2 g^{-1}$) and pore volume (1 $cm^3 g^{-1}$) while relatively low values are obtained for Co–B oxide (Cl^-) sample (93 $m^2 g^{-1}$, 0.33 $cm^3 g^{-1}$).

The evaluation of XPS survey scans, as well as bulk EDX analysis suggest a chemical composition that consists mainly of Co, B, and O as expected (Figure S23–26). The Co 2p regions shown in Figure 6e exhibit the characteristic peaks of Co^{2+} and Co^{3+} for all three samples. To make a fair comparison on the ratio of Co^{2+}/Co^{3+} among these oxides, we utilize the integrated area of satellite peaks of Co^{2+} and Co^{3+}, which are located at 785.7 eV and 789.6 eV, respectively (fitted XPS spectra are provided in Figure S27). It is obvious to see that Co–B oxide (SO_4^{2-}) and Co–B oxide (Cl^-) contain a higher amount of Co^{2+} on the surface as one could expect for stoichiometric Co_3O_4. Regarding the B 1s spectrum, only one peak corresponding to a B-oxo bond is observed (Figure 6f). This is consistent with the previous suggestion, that B forms B_2O_3 after calcination in air. Furthermore, we compare the surface Co/B ratios of four Co–B oxides based on XPS results.

Based on these structure characterizations, we were able to correlate the amount of boron on the surface with some structural properties. First, oxides with higher B content possess larger surface areas and pore volumes, suggesting the protective role of boron-containing phase that slows down particle aggregation and preserves the sintering by keeping the structure and high surface area. Second, the sample containing higher amounts of B seems to correlate with a higher average oxidation state of the Co site, which can be a result of interactions between B_2O_3 and Co_3O_4 interfaces. The synergistic effect of boron is further reflected in the catalytic behaviour of cobalt oxide catalysts. As shown in Figure 6g–h, among four Co–B oxide samples prepared by using different precursors, the samples with higher boron contents are much more active OER catalysts, in terms of delivering a higher current density as well as a lower Tafel slope. The superior activity is resulted from a collective contribution of (a) larger surface area exposing to reactant species as well as (b) the stabilization of surface Co species. Although Co–B oxide (Ac^-) and Co–B oxide (NO_3^-) provide similar surface area, the relatively higher OER activity of Co–B oxide (Ac^-) can be attributed to a slightly small charge transfer resistance during the electrochemical reaction (Figure 6i).

Conclusion

In summary, we have fabricated a series of Co–B oxides with tunable morphology, crystallinity and textural parameters via a facile precipitation method under air atmosphere. The detailed characterization and structural analyses support the formation of a mixture of different Co–B-oxides and hydroxides after precipitation and the temperature-induced formation of Co_3O_4 and a boron containing oxide such as for example B_2O_3 as well as the presence of structural defects. The existence of boron was found to influence not only the morphology, crystallization and surface structure of the final oxide, it also significantly affects its OER performance. This synergy resulted in a three-fold increment in the OER activity of Co–B oxide, in comparison with reference ordered mesoporous Co_3O_4 counterparts. Among the Co–B oxides, a partially crystalline sample that was calcined at 300 °C exhibited the highest catalytic performance towards OER by delivering a current density of 235 $mA cm^{-2}$ at 1.7 V_{RHE} and requiring an overpotential of 338 mV to reach 10 $mA cm^{-2}$. Identical location TEM and in situ electrochemical Raman spectroscopy studies show the alteration and surface re-construction of the materials. The formation of CoO_2 and (oxy)hydroxide intermediates during OER were found to be highly dependent on the crystallinity of the samples. This simplified method can be applied to adjust morphology, textural parameters as well as the boron amount by varying cobalt precursors.

Acknowledgements

We thank the Max Planck Society for the basic funding. This study was financially supported by IMPRS-RECHARGE, SURMAT and FUNCAT of the Max Planck Society, the Volkswagen Foundation (96_742) and the Deutsche Forschungsgemeinschaft (DFG, German Research Foundation) Projektnummer 388390466-TRR 247 within the Collaborative Research Centre/Transregio 247 "Heterogeneous Oxidation Catalysis in the Liquid Phase". S. Palm, H. Bongard, A. Schlüter, and N. Pfänder are acknowledged for EDX analysis and electron microscopy images. We gratefully thank J. N. Büscher and S. Leiting for conducting XPS measurements. We acknowledge DESY (Hamburg, Germany) as a member of the Helmholtz Association HGF, for the provision of experimental facilities. Parts of this research were carried out at PETRA III, beamline P02.1 (proposal I-20190175) and we thank M. Etter for assistance during beamtime. We acknowledge Diamond Light Source for time on beamline I20-scanning under proposal SP21526. XAS data were collected at the Soleil synchrotron, the L-edges at the Sextants beamline (proposal 20181522) and the K-edge at the Samba beamline (proposal 20201215). We thank M. Aramini (I-20), A. Nicolaou (Sextants) and G. Landrot (Samba) for assistance during the respective beamtimes. Open Access funding enabled and organized by Projekt DEAL.

 © 2022 The Authors. Angewandte Chemie International Edition published by Wiley-VCH GmbH

Conflict of Interest

The authors declare no conflict of interest.

Data Availability Statement

The data that support the findings of this study are available from the corresponding author upon reasonable request.

Keywords: Co_3O_4 · Oxygen Evolution Reaction · Surface Boron Oxide · Water Electrolysis

[1] a) S. Chu, Y. Cui, N. Liu, *Nat. Mater.* **2017**, *16*, 16–22; b) N. S. Lewis, D. G. Nocera, *Proc. Natl. Acad. Sci. USA* **2006**, *103*, 15729–15735; c) M. Yu, E. Budiyanto, H. Tüysüz, *Angew. Chem. Int. Ed.* **2022**, *61*, e202103824; *Angew. Chem.* **2022**, *134*, e202103824.

[2] a) P. Nikolaidis, A. Poullikkas, *Renewable Sustainable Energy Rev.* **2017**, *67*, 597–611; b) S. Klemenz, A. Stegmuller, S. Yoon, C. Felser, H. Tüysüz, A. Weidenkaff, *Angew. Chem. Int. Ed.* **2021**, *60*, 20094–20100; *Angew. Chem.* **2021**, *133*, 20254–20260.

[3] C. C. McCrory, S. Jung, I. M. Ferrer, S. M. Chatman, J. C. Peters, T. F. Jaramillo, *J. Am. Chem. Soc.* **2015**, *137*, 4347–4357.

[4] I. Roger, M. A. Shipman, M. D. Symes, *Nat. Chem. Rev.* **2017**, *1*, 0003.

[5] a) F. Song, L. Bai, A. Moysiadou, S. Lee, C. Hu, L. Liardet, X. Hu, *J. Am. Chem. Soc.* **2018**, *140*, 7748–7759; b) B. M. Hunter, H. B. Gray, A. M. Muller, *Chem. Rev.* **2016**, *116*, 14120–14136; c) M. Yu, G.-H. Moon, E. Bill, H. Tüysüz, *ACS Appl. Energy Mater.* **2019**, *2*, 1199.

[6] a) X. H. Deng, H. Tüysüz, *ACS Catal.* **2014**, *4*, 3701–3714.

[7] R. Subbaraman, D. Tripkovic, K. C. Chang, D. Strmcnik, A. P. Paulikas, P. Hirunsit, M. Chan, J. Greeley, V. Stamenkovic, N. M. Markovic, *Nat. Mater.* **2012**, *11*, 550–557.

[8] J. Suntivich, K. J. May, H. A. Gasteiger, J. B. Goodenough, Y. Shao-Horn, *Science* **2011**, *334*, 1383–1385.

[9] a) J. Masa, W. Schuhmann, *ChemCatChem* **2019**, *11*, 5842–5854; b) K. Xu, P. Chen, X. Li, Y. Tong, H. Ding, X. Wu, W. Chu, Z. Peng, C. Wu, Y. Xie, *J. Am. Chem. Soc.* **2015**, *137*, 4119–4125; c) P. Chen, T. Zhou, M. Zhang, Y. Tong, C. Zhong, N. Zhang, L. Zhang, C. Wu, Y. Xie, *Adv. Mater.* **2017**, *29*, 1701584–1701589; d) N. Han, K. R. Yang, Z. Lu, Y. Li, W. Xu, T. Gao, Z. Cai, Y. Zhang, V. S. Batista, W. Liu, X. Sun, *Nat. Commun.* **2018**, *9*, 924–933; e) Q. Gao, C.-Q. Huang, Y.-M. Ju, M.-R. Gao, J.-W. Liu, D. An, C.-H. Cui, Y.-R. Zheng, W.-X. Li, S.-H. Yu, *Angew. Chem. Int. Ed.* **2017**, *56*, 7769–7773; *Angew. Chem.* **2017**, *129*, 7877–7881.

[10] a) D. Li, H. Baydoun, C. N. Verani, S. L. Brock, *J. Am. Chem. Soc.* **2016**, *138*, 4006–4009; b) P. W. Menezes, A. Indra, I. Zaharieva, C. Walter, S. Loos, S. Hoffmann, R. Schlögl, H. Dau, M. Driess, *Energy Environ. Sci.* **2019**, *12*, 988–999; c) J. M. V. Nsanzimana, Y. C. Peng, Y. Y. Xu, L. Thia, C. Wang, B. Y. Xia, X. Wang, *Adv. Energy Mater.* **2018**, *8*, 1701475.

[11] a) F. Guo, Y. Wu, H. Chen, Y. Liu, L. Yang, X. Ai, X. Zou, *Energy Environ. Sci.* **2019**, *12*, 684–692; b) P. W. Menezes, C. Panda, C. Walter, M. Schwarze, M. Driess, *Adv. Funct. Mater.* **2019**, *29*, 1808632.

[12] M. W. Kanan, D. G. Nocera, *Science* **2008**, *321*, 1072–1075.

[13] J. Park, H. Kim, K. Jin, B. J. Lee, Y. S. Park, H. Kim, I. Park, K. D. Yang, H. Y. Jeong, J. Kim, K. T. Hong, H. W. Jang, K. Kang, K. T. Nam, *J. Am. Chem. Soc.* **2014**, *136*, 4201–4211.

[14] H. Kim, J. Park, I. Park, K. Jin, S. E. Jerng, S. H. Kim, K. T. Nam, K. Kang, *Nat. Commun.* **2015**, *6*, 8253.

[15] Y. Shao, X. Xiao, Y. P. Zhu, T. Y. Ma, *Angew. Chem. Int. Ed.* **2019**, *58*, 14599–14604; *Angew. Chem.* **2019**, *131*, 14741–14746.

[16] L. Yang, Z. Guo, J. Huang, Y. Xi, R. Gao, G. Su, W. Wang, L. Cao, B. Dong, *Adv. Mater.* **2017**, *29*, 1704574.

[17] S. Sun, X. Zhou, B. Cong, W. Hong, G. Chen, *ACS Catal.* **2020**, *10*, 9086–9097.

[18] Q. Fu, T. Wu, G. Fu, T. Gao, J. Han, T. Yao, Y. Zhang, W. Zhong, X. Wang, B. Song, *ACS Energy Lett.* **2018**, *3*, 1744–1752.

[19] P. F. Liu, X. Li, S. Yang, M. Y. Zu, P. R. Liu, B. Zhang, L. R. Zheng, H. J. Zhao, H. G. Yang, *ACS Energy Lett.* **2017**, *2*, 2257–2263.

[20] a) J. Masa, P. Weide, D. Peeters, I. Sinev, W. Xia, Z. Sun, C. Somsen, M. Muhler, W. Schuhmann, *Adv. Energy Mater.* **2016**, *6*, 1502313; b) H. Liu, L. Yang, K. Qiao, L. Zheng, X. Cao, D. Cao, *ChemSusChem* **2019**, *12*, 3524–3531.

[21] D. K. Bediako, Y. Surendranath, D. G. Nocera, *J. Am. Chem. Soc.* **2013**, *135*, 3662–3674.

[22] a) T. Grewe, X. H. Deng, C. Weidenthaler, F. Schüth, H. Tüysüz, *Chem. Mater.* **2013**, *25*, 4926–4935; b) M. Yu, C. K. Chan, H. Tüysüz, *ChemSusChem* **2018**, *11*, 605–611.

[23] D. Cabrera-German, G. Gomez-Sosa, A. Herrera-Gomez, *Surf. Interface Anal.* **2016**, *48*, 252–256.

[24] M. A. Langell, M. D. Anderson, G. A. Carson, L. Peng, S. Smith, *Phys. Rev. B* **1999**, *59*, 4791–4798.

[25] S. C. Petitto, E. M. Marsh, G. A. Carson, M. A. Langell, *J. Mol. Catal. A* **2008**, *281*, 49–58.

[26] J. Stuart, A. Hohenadel, X. Li, H. Xiao, J. Parkey, C. P. Rhodes, S. Licht, *J. Electrochem. Soc.* **2015**, *162*, A192–A197.

[27] W. A. Brainard, D. R. Wheeler, *J. Vac. Sci. Technol.* **1978**, *15*, 1800–1805.

[28] E. Onur Şahin, H. Tüysüz, C. K. Chan, G.-H. Moon, Y. Dai, W. Schmidt, J. Lim, C. Scheu, C. Weidenthaler, *Nanoscale* **2021**, *13*, 150–162.

[29] A. M. Hibberd, H. Q. Doan, E. N. Glass, F. M. F. de Groot, C. L. Hill, T. Cuk, *J. Phys. Chem. C* **2015**, *119*, 4173–4179.

[30] a) P. Glatzel, U. Bergmann, *Coord. Chem. Rev.* **2005**, *249*, 65–95; b) C. J. Pollock, M. U. Delgado-Jaime, M. Atanasov, F. Neese, S. DeBeer, *J. Am. Chem. Soc.* **2014**, *136*, 9453–9463.

[31] R. G. Castillo, A. W. Hahn, B. E. Van Kuiken, J. T. Henthorn, J. McGale, S. DeBeer, *Angew. Chem. Int. Ed.* **2021**, *60*, 10112–10121; *Angew. Chem.* **2021**, *133*, 10200–10209.

[32] E. Budiyanto, M. Q. Yu, M. M. Chen, S. DeBeer, O. Rudiger, H. Tüysüz, *ACS Appl. Energy Mater.* **2020**, *3*, 8583–8594.

[33] M. Yu, G. H. Moon, R. G. Castillo, S. DeBeer, C. Weidenthaler, H. Tüysüz, *Angew. Chem. Int. Ed.* **2020**, *59*, 16544–16552; *Angew. Chem.* **2020**, *132*, 16687–16695.

[34] S. Jung, C. C. L. McCrory, I. M. Ferrer, J. C. Peters, T. F. Jaramillo, *J. Mater. Chem. A* **2016**, *4*, 3068–3076.

[35] D. G. Tong, D. Wang, W. Chu, J. H. Sun, P. Wu, *Electrochim. Acta* **2010**, *55*, 2299–2305.

[36] a) J. Huang, H. Sheng, R. D. Ross, J. Han, X. Wang, B. Song, S. Jin, *Nat. Commun.* **2021**, *12*, 3036; b) M. Kitajima, *Crit. Rev. Solid State Mater. Sci.* **1997**, *22*, 275–349.

[37] C. Pasquini, L. D'Amario, I. Zaharieva, H. Dau, *J. Chem. Phys.* **2020**, *152*, 194202.

[38] J. Yang, H. W. Liu, W. N. Martens, R. L. Frost, *J. Phys. Chem. C* **2010**, *114*, 111–119.

[39] K. H. Gayer, A. B. Garrett, *J. Am. Chem. Soc.* **1950**, *72*, 3921–3923.

[40] a) A. Moysiadou, S. Lee, C.-S. Hsu, H. M. Chen, X. Hu, *J. Am. Chem. Soc.* **2020**, *142*, 11901–11914; b) Z. Chen, L. Cai, X. Yang, C. Kronawitter, L. Guo, S. Shen, B. E. Koel, *ACS Catal.* **2018**, *8*, 1238–1247; c) N. Kornienko, N. Heidary, G. Cibin, E. Reisner, *Chem. Sci.* **2018**, *9*, 5322–5333.

© 2022 The Authors. Angewandte Chemie International Edition published by Wiley-VCH GmbH

[41] a) E. Budiyanto, S. Salamon, Y. Wang, H. Wende, H. Tüysüz, *JACS Au* **2022**, *2*, 697–710; b) Y. C. Liu, J. A. Koza, J. A. Switzer, *Electrochim. Acta* **2014**, *140*, 359–365.
[42] R. Shannon, *Acta Crystallogr. Sect. A* **1976**, *32*, 751–767.
[43] W. Cai, R. Chen, H. Yang, H. B. Tao, H.-Y. Wang, J. Gao, W. Liu, S. Liu, S.-F. Hung, B. Liu, *Nano Lett.* **2020**, *20*, 4278–4285.
[44] C. C. L. McCrory, S. Jung, J. C. Peters, T. F. Jaramillo, *J. Am. Chem. Soc.* **2013**, *135*, 16977–16987.
[45] S. Möller, S. Barwe, J. Msa, D. Wintrich, S. Seisel, H. Baltruschat, W. Schuhmann, *Angew. Chem. Int. Ed.* **2020**, *59*, 1585–1589; *Angew. Chem.* **2020**, *132*, 1601–1605.
[46] B. S. Yeo, A. T. Bell, *J. Am. Chem. Soc.* **2011**, *133*, 5587–5593.
[47] J. M. V. Nsanzimana, L. Q. Gong, R. Dangol, V. Reddu, V. Jose, B. Y. Xia, Q. Y. Yan, J. M. Lee, X. Wang, *Adv. Energy Mater.* **2019**, *9*, 1901503.

Manuscript received: August 5, 2022
Accepted manuscript online: August 24, 2022
Version of record online: September 12, 2022

© 2022 The Authors. Angewandte Chemie International Edition published by Wiley-VCH GmbH